Metabolic heterogeneity of colorectal cancer as a prognostic factor: insights gained from fluorescence lifetime imaging

Anastasia D Komarova[1,2†], Snezhana D Sinyushkina[1†], Ilia D Shchechkin[1,2], Irina N Druzhkova[1], Sofia A Smirnova[1], Vitaliy M Terekhov[3], Artem M Mozherov[1], Nadezhda I Ignatova[1], Elena E Nikonova[4], Evgeny A Shirshin[4,5], Vladislav I Shcheslavskiy[1,6], Marina V Shirmanova[1*]

[1]Institute of Experimental Oncology and Biomedical Technologies, Privolzhsky Research Medical University, Nizhny Novgorod, Russia; [2]Institute of Biology and Biomedicine, Lobachevsky State University of Nizhny Novgorod, Nizhny Novgorod, Russia; [3]Surgery department, Nizhny Novgorod Regional Oncologic Hospital, Nizhny Novgorod, Russia; [4]Laboratory of Clinical Biophotonics, Sechenov First Moscow State Medical University, Moscow, Russia; [5]Faculty of Physics, Lomonosov Moscow State University, Moscow, Russia; [6]Becker&Hickl GmbH, Germany

***For correspondence:** Shirmanovam@gmail.com

[†]These authors contributed equally to this work

Competing interest: The authors declare that no competing interests exist

Abstract

Heterogeneity of tumor metabolism is an important, but still poorly understood aspect of tumor biology. Present work is focused on the visualization and quantification of cellular metabolic heterogeneity of colorectal cancer using fluorescence lifetime imaging (FLIM) of metabolic cofactor NAD(P)H. FLIM-microscopy of NAD(P)H was performed in vitro in four cancer cell lines, in vivo in the four types of tumors in mice and ex vivo in patients' tumor samples. The dispersion and bimodality of the decay parameters were evaluated to quantify the intercellular metabolic heterogeneity. Our results demonstrate that patients' tumors have significantly higher heterogeneity of metabolism compared with cultured cells and tumor xenografts. It was found that dispersion of a contribution of a free fraction of NAD(P)H is higher in the high-grade tumors, and the bimodality in a distribution of the free NAD(P)H fraction has associations with tumor metastasis. These results indicate that cell-level metabolic heterogeneity assessed from NAD(P)H FLIM has a potential to become a clinical prognostic factor.

Key words: Fluorescence lifetime imaging, FLIM, colorectal adenocarcinoma, tumor metabolism, metabolic heterogeneity, NAD(P)H, autofluorescence

Introduction

Reprogramming of energy metabolism is an established hallmark of malignant tumors. Tumor cells adjust their metabolism to sustain uncontrolled proliferation and tumor progression, even in the conditions of low nutrient supply and hypoxia. There are two main metabolic pathways for energy production in the form of ATP – glycolysis and oxidative phosphorylation (OXPHOS). For a long time, enhanced glycolysis has been considered as a central feature of tumor metabolism (DeBerardinis and Chandel, 2016). Unlike most normal cells, tumor cells rely on glycolysis not only in hypoxia (anaerobic glycolysis), but also in normoxia (aerobic glycolysis, or the Warburg effect), which provides them with many metabolic intermediates and a high-speed production of ATP for fast growth. The glycolytic shift in the tumors traditionally correlates with negative prognosis (Zhou et al., 2022). At the same time, mitochondrial OXPHOS is as important in malignant cells as glycolysis. Although defective mitochondria and lower OXPHOS capacity are often observed in cancer cells, this is not an absolute phenomenon – many tumors preserve functional mitochondria and normal OXPHOS rate (Gentric et al., 2017). Along with glucose, tumors use glutamine and fatty acids as alternative substrates. Interestingly, tumor cells are capable of switching between different metabolic pathways depending on their own needs and local environment, thus demonstrating a high degree of metabolic plasticity.

Therefore, tumor metabolism is currently viewed as a dynamic, variable system with a diversity of cellular metabolic states. In this context, intratumor heterogeneity means that there are the cells with different metabolic profiles in a tumor concurrently, and intertumor heterogeneity means that tumors of the same type and stage are characterized by the different metabolic strategies (Kim and DeBerardinis, 2019).

Heterogeneity of tumor metabolism can be caused by various factors (Shirmanova et al., 2023). Some of them («intrinsic») are related to tumor cells themselves: these are histogenesis of the tumor, mutation profile, (epi)genetics factors, differentiation state and proliferation activity, to name a few (Pavlova and Thompson, 2016; Sengupta and Pratx, 2016; Seth Nanda et al., 2020; Farhadi et al., 2022). Other reasons («extrinsic») are associated with the nonuniform microenvironment, e.g., local hypoxia, nutrient distribution, heterogeneity of the vasculature network, interaction of tumor cells with the extracellular matrix and stromal cells, etc. (Marusyk and Polyak, 2010; Masson and Ratcliffe, 2014; Yoshida, 2015; Stine et al., 2015). Collectively, these factors lead to variability of tumor metabolism in space and time. Metabolic heterogeneity as a part of general heterogeneity of tumors imposes some difficulties in patients' diagnosis and treatment and is believed to have a prognostic value.

Although metabolic heterogeneity is a well-recognized feature of tumors, its characterization at the cellular level remains scarce. In part, this is associated with the lack of the highly sensitive and direct techniques for its observation. Clinical imaging modalities, such as metabolic PET with radiolabeled tracers (^{18}F, ^{11}C) and MRI/MRS, allow to capture inter- and intratumor heterogeneity among patients with low (~4.5 mm) spatial resolution (Plathow and Weber, 2008). Recently evolved methods of single-cell sequencing deliver comprehensive information about the metabolic landscape of a tumor with a resolution up to 55–100 µm based on the expression of the metabolic genes, but these approaches are rather complex, laborious and not widely available (Evers et al., 2019; Huang et al., 2023).

Interrogation of cellular metabolism is possible with the laser scanning fluorescence microscopy that enables the detection of autofluorescence of the redox cofactors, such as the reduced form of the nicotinamide adenine dinucleotide (phosphate) – NAD(P)H and oxidized flavins (Georgakoudi and Quinn, 2023). Recording of the fluorescence decay parameters using the option of the fluorescence lifetime imaging (FLIM) allows the evaluation of the states of the cofactor molecules attributed to different metabolic pathways. Specifically, the unbound state of NAD(P)H has a short lifetime (~0.4 ns) and is associated with glycolysis, while the protein-bound state has a long lifetime (~1.7–3.0 ns) and is associated with OXPHOS (Lakowicz et al., 1992). FLIM of NAD(P)H is currently considered as a promising, label-free technique for the assessment of metabolic heterogeneity of tumors at the (sub)cellular scale. Several studies, including ours, demonstrate the possibilities of NAD(P)H FLIM to visualize metabolic heterogeneity in cultured cells, multicellular structures in vitro, tumor xenografts in vivo and patients' tumors ex vivo (Shah et al., 2015; Skala et al., 2022; Lukina et al., 2019). However, quantifying the degree of tumor heterogeneity is lacking in most of these works.

In this paper, we present the results of assessment of cell-level metabolic heterogeneity of colorectal cancer using FLIM-microscopy of NAD(P)H. The distributions of the fluorescence decay parameters have been analyzed in the four colorectal cancer cell lines (HT29, HCT116, CaCo2, CT26), in the mouse tumor models in vivo generated from these cell lines and in the post-operative samples of patients' colon tumors. Quantification of heterogeneity has been performed with the dispersion and the bimodality index (BI) of the decay parameter a_1 (contribution of free NAD(P)H). Correlative analysis has been conducted to find associations of the heterogeneity degree with clinical prognosis.

Results

1. Metabolic heterogeneity assessment in colorectal cancer cell lines

First, using FLIM of NAD(P)H, cellular metabolism was assessed in monolayer cultures of different colorectal cancer cell lines (Figure 1A). Typical values of NAD(P)H fluorescence

lifetimes were registered for all cell lines – short τ_1 ~0.39 ns and long τ_2 ~2.30–2.90 ns (Table S1). Due to specifics of cellular metabolism, the relative contributions of the free (a_1) and bound (a_2) forms of NAD(P)H and, consequently, the mean lifetimes τ_m varied between the cell lines. The a_1 value decreased and τ_m increased in the following order: CT26 (~86%, 0.57 ns) > HCT116 (~84%, 0.71 ns) > HT29 (~80%, 0.80 ns) > CaCo2 (~73%, 0.94 ns) (Figure 1B, Table S1). A high NAD(P)H-a_1 (low τ_m) is an indicator of glycolytic shift, which is typical for cells with intense proliferation in a monolayer culture, like CT26 and HCT116. CaCo2 cells with the lowest a_1 value had more OXPHOS-shifted metabolism, which can be associated with the expression of morphological and functional characteristics of mature enterocytes of normal small intestine by this cell line (Lea, 2015). In all cell lines inter-cellular variations of the a_1 parameter were minor (<3%).

To quantify the metabolic heterogeneity, the BI was calculated for distributions of both a_1 (Figure 1C) and τ_m values (Figure S1). For all cell lines, except CaCo2, the BI of the a_1 distribution did not exceed 1.1 (the threshold of bimodality), justifying the uniformity of cell metabolism in a culture, which is consistent with the general view on standard cell lines as homogenous populations. CaCo2 cell culture appeared bimodal in a_1 parameter (BI-a_1=1.12), which is rational because this cell line is known to be heterogeneous and contain cells of a colon carcinoma and differentiated cells with properties of mature enterocytes (Lea, 2015). The BI-τ_m was, however, rather high (>1.0) in all cell lines except HCT116 (0.84). In the further experiments on tumors and tissue samples the BI-a_1 was used as more relevant.

Additionally, the dispersion of NAD(P)H-a_1 (D-a_1) was evaluated for each cell line to describe the extent of distribution of the data around the median (Table 1). The D-a_1 value varied from 1.67% in CT26 cell culture to 3.5% in CaCo2.

2. Metabolic heterogeneity in mouse tumor models in vivo

Next, FLIM of NAD(P)H was performed in vivo on mouse tumor models, obtained from the colorectal cell lines shown above (Figure 2A). All the tumors were verified by histopathological analysis (Figure 2B).

Among the tumors, CT26 had the highest (~83%), and CaCo2 had, on average, the lowest (~76%) contribution of free NAD(P)H a_1, similar to the cultured cells (Figure 2C, Table S1).

Most of the individual tumors showed larger (≥3%) inter-cellular variations of NAD(P)H-a_1 than corresponding cell lines, where the deviation from the median was ≤3%. The dispersion D-a_1 was in the range of 2.6–4.02%, and for each specific tumor type was higher than in the corresponding cell line (Table 1). At that, intertumor differences across each type of tumor were insignificant.

The BI-a_1 values in mouse tumors were generally higher than in monolayer cultures (Figure 2D, Table 1). In 4 of 12 tumors the BI-a_1 was ≥1.1, indicating the bimodal distribution of the a_1 parameter, i.e., the presence of two subpopulations of cells with different metabolism. Seven tumors had the BI-a_1 in the range of 0.7–1.0, which suggests that, while the distribution of the estimated parameter was unimodal, it was either wide or asymmetric, thus, also indicating some degree of heterogeneity. In 1 of 12 tumors the BI-a_1 was small (0.23), suggesting uniformity of cells' metabolism. Given the genetic identity of cells in standard cell lines, we can assume that the nonuniform microenvironment in the tumors was a major source of their variable metabolism.

To ensure that the observed heterogeneity resulted from the diversity of cancer cells but not from the contribution of stromal cells, that cannot be reliably identified on NAD(P)H FLIM images, immunohistochemical staining for EpCam (epithelial marker) and vimentin (mesenchymal marker) was performed. It was found that in tumor xenografts the fraction of cells stained with vimentin was less than 10% (Figure S2).

3. Metabolic heterogeneity in colorectal cancer samples from patients

NAD(P)H FLIM images were collected from 21 postoperative samples of patients' colorectal adenocarcinomas, among which were the tumors of the I–IV stages, poorly and highly differentiated. The representative FLIM and histological images are presented in Figure 3A and B correspondingly. Patients' tumors showed fluorescence lifetimes of τ_1 ~0.45 ns and τ_2 ~1.80–3.20 ns (Table S3), which were comparable with the values in human tumor xenografts (Table S1). The parameter NAD(P)H-a_1 was in the range of ~62–80% and NAD(P)H-τ_m was in the range of 0.80–1.20 ns, indicating that patients' tumors generally had larger variability of metabolic statuses than cancer cells in vitro and in xenografts in vivo.

A high degree of inter- and intratumor variability of cellular metabolism was detected in patients' tumors (Figure 3C). Half of the tumors (10 of 21) showed deviation of NAD(P)H-a_1 from the median <10% across the cells, and for the rest (11 of 21) the variations were 10–25%. The dispersion D-a_1 varied significantly among the samples, from 2.19% to 11.99%.

According to the heterogeneity assessment using the bimodality index, 9 of 21 tumors were metabolically highly heterogeneous (BI-a_1≥1.1) (Figure 3D). In 11 tumors the BI-a_1 value was in the range of 0.59–1.0, which indicated the presence of metabolically different cells but not clearly separated into two clusters. Only one tumor sample (p16) was metabolically homogeneous (BI-a_1=0.24).

Notably, the bimodality index showed no correlation with dispersion. That is, among the samples there were those with bimodal distribution, but small dispersion of NAD(P)H-a_1 in a cell population (e.g., p12, p13, p21), and vice versa (e.g., p3, p7, p8).

Therefore, using NAD(P)H FLIM we have observed and quantified metabolic heterogeneity of patients' colorectal tumors. Unlike tumor xenografts obtained from the cell lines that are thought to be genetically stable and identical, patients' tumors are genetically diverse, which could also contribute to their metabolic heterogeneity, in addition to microenvironmental factors.

4. Interrelation between metabolic heterogeneity and clinicopathological characteristics of tumors

The relationships between the metrics of cellular heterogeneity BI-τ_m, BI-a_1 and the D-a_1 NAD(P)H with the clinical parameters of the tumor, such as the stage according to the TNM system and the grade (G), were analyzed. Due to the small sample size, all tumors were divided into two groups by each parameter: T1+T2 and T3+T4; N0M0 and all the others with metastases; G1+G2 and G3.

The results showed that the high-grade tumors displayed a higher value of dispersion of NAD(P)H-a_1 than the low-grade ones, indicating their higher heterogeneity (Figure 4). R point-biserial correlation coefficient between the grade and the dispersion a_1 was -0.49 (p-val = 0.03). Thus, the dispersion of free NAD(P)H fraction a_1 allowed differentiating between the low-grade and high-grade tumors with a high accuracy (p-val = 0.01).

Tumors of the advanced stages T3 and T4 were characterized by reduced dispersion of D-a_1 and increased bimodality index BI-a_1 compared with early stages T1 and T2 (Figure 4). The stage of the tumor T has a tendency to be associated with D-a_1 (p-val = 0.06); the correlation between T stage and D-a_1 was -0.43 (p-val = 0.04).

Importantly, if metastases were present (N and M were different from 0 in TNM), then those primary tumors showed higher values of the bimodality index BI-a_1 compared with tumors for which metastases were absent (Figure 4). The NM parameter had a significant trend of association with BI-a_1 (p-val = 0.07), although the dispersion of a_1 for metastatic tumors was low.

We also note that the BI-τ_m had no significant associations with clinicopathological parameters of the tumors (Figure S3).

Discussion

The altered energy metabolism is known to support tumor progression because tumor cells are critically in need of ATP for uncontrolled proliferation and growth. It has been established that tumor cells explore different metabolic programs and utilize multiple fuels even within one tumor, thus leading to metabolic heterogeneity. Until recently, direct observation of cell-level heterogeneity of tumor metabolism was a challenging task, but became possible with the evolution of advanced optical microscopic techniques, such as two-photon fluorescence

lifetime microscopy, FLIM. In the present research, using FLIM of metabolic cofactor NAD(P)H, which possesses endogenous fluorescence, we compared metabolic features of colorectal cancer cells across in vitro and in vivo models and patients' samples. For the first time, the heterogeneity of cellular metabolism quantified on the basis of FLIM data was correlated with clinical characteristics of the tumors.

A lot of studies, including the works of our group, demonstrate the possibilities of FLIM for assessment of the intra- and intertumor heterogeneity of metabolism in different models. Using NAD(P)H FLIM, metabolic heterogeneity was revealed in colorectal cancer cell cultures obtained from the patients' tumors, whereas the cells of the standard cell lines were uniform in their metabolism (Shirshin et al., 2022). J. Chacko and K. Eliceiri observed intercellular heterogeneity of metabolism in the MCF10A human breast epithelial cell line (Chacko and Eliceiri, 2019). Several studies show metabolic heterogeneity of 3D multicellular structures. For example, tumor spheroids obtained from the cervical cancer cell line HeLa (Lukina et al., 2018) or murine colorectal carcinoma cell line CT26 (Shirmanova et al., 2021) displayed the differences in metabolism between the outer and the inner cell layers with the outer layers being more glycolytic (higher NAD(P)H-a_1). The spheroids generated from the patients' derived glioblastoma cultures did not show metabolic zonality, but generally had greater intercellular variations of NAD(P)H lifetime parameters than the spheroids from standard line U373 MG (Yuzhakova et al., 2023). A spectrum of works by M. Skala' group demonstrates an opportunity of the optical metabolic imaging for heterogeneity assessment in patient tumor-derived organoids on the example of a breast, pancreatic (Sharick et al., 2020; Walsh et al., 2014; Walsh et al., 2017), head and neck (Shah et al., 2017), colorectal cancers (Skala et al., 2022).

In the research in vivo, the heterogeneous structure of tumor and its microenvironment was shown on PyMT mammary tumors (Burkel et al., 2022). Analysis of the optical metabolic parameters revealed heterogeneity of the B78 mouse melanoma model, caused by different microenvironments (Heaton et al., 2023). The authors suggested that tumor heterogeneity could be induced by such factors as pH, nutrient and oxygen availability, or activation of immune cells. In the in vivo study on HeLa tumor xenografts, metabolically different cells were detected in the cellular and collagen-rich areas (Shirmanova et al., 2018). Recently, we demonstrated a high variability of cellular metabolic statuses in CT26 tumors of large size compared with small tumors, which correlated with heterogeneous oxygen distribution (Parshina et al., 2022). A significant intertumor heterogeneity of metabolism was observed in patient-derived glioblastoma xenografts, which differed them from standard U87 glioma (Yuzhakova et al., 2022).

In our study, we compared metabolic FLIM parameters of colorectal cell lines, mouse tumor models and patients' colorectal tumors. As expected, intercellular heterogeneity of

metabolism was the highest in patients' tumor samples as followed from a wide and often bimodal distribution of NAD(P)H-a_1. This result is consistent with the study by J. Auman and H. McLeod using genome-wide gene expression data; the authors concluded that colorectal cancer cell lines lack the molecular heterogeneity of clinical colorectal tumors (Auman and McLeod, 2010).

Cell-level metabolic heterogeneity may be present in the cell population initially, as discussed above, or develop during the treatment. The heterogeneous metabolism after treatment was detected in tumor organoids (Walsh et al., 2016; Walsh et al., 2014; Gillette et al., 2021) and in animal models (Heaster et al., 2019). In any case, the presence of metabolically distinct cells led to the varying drug responses.

An assessment of metabolic heterogeneity in patients' tumors seems valuable from a clinical point of view. Previously, using NAD(P)H FLIM of postoperative samples, we observed a high degree of inter- and intratumor heterogeneity of T3 stage colorectal tumors in comparison with normal colon samples (Lukina et al., 2019). Unfortunately, most of the tumor types are inaccessible for microscopic investigation in patients using clinically approved techniques. The exception is the skin tumors that can be inspected with clinical systems, like MPTflex or MPTcompact (JenLab, Germany). At the same time, endoscopic FLIM-microscopy has been developing actively since the last ten years, which opens the prospects for in vivo examination of a wide spectrum of patients' tumor types (Sun et al., 2013; Farhadi et al., 2022). In principle, an assessment of tumor metabolism in biopsy samples is also possible, which widens the potential clinical applications of FLIM.

Although metabolic heterogeneity at the cellular level has been reported for different models and patient-derived cells, the comparisons between different samples and studies are hard to make as most of them lack any quantification of the heterogeneity.

Different approaches have been proposed to quantify the metabolic differences identified by FLIM. For example, in the papers (Shah et al., 2015; Sharick et al., 2019) a heterogeneity index and its modified form the weighted heterogeneity index (wH-index) were used for quantitative analysis of cellular heterogeneity. The wH-index is based on the Gaussian distribution models and is a modified form of the Shannon diversity index. Using this index the authors described the variations of a combination of parameters, such as NAD(P)H fluorescence lifetime, FAD fluorescence lifetime and optical redox ratio, defined as the OMI-index. The methods developed in Ref. (Heaster et al., 2019) established the combination of optical metabolic imaging variables and spatial statistical analysis (spatial proximity analysis, spatial clustering, multivariate spatial analysis, spatial principal components analysis) to quantify the spatial heterogeneity of tumor cell metabolism. Recently, we have proposed a new quantitative

criterion – the bimodality index (BI) – to accurately discriminate between metabolically diverse cellular subpopulations on the basis of NAD(P)H FLIM data (Shirshin et al., 2022). The BI provides dimensionless estimation on the inherent heterogeneity of a sample by checking the hypothesis about approximation of a fluorescence decay parameter distribution by two Gaussians. Using the BI, the metabolic heterogeneity has been identified in standard and primary cancer cells cultures after chemotherapy with 5-fluorouracil. Here, we used the dispersion of NAD(P)H-a_1 and BI-a_1 for quantifying metabolic heterogeneity of patient's tumors and compared it with in vitro and in vivo models.

Metabolic heterogeneity of colorectal cancer is also discussed in the literature. The focus of many of these studies is on the molecular classification of tumors by the analysis of their metabolic features. For example, Zhang et al. showed that colorectal tumors could be classified into three distinct metabolism-relevant subtypes and developed a metabolism-related signature consisting of 27 metabolic genes, which were expressed differentially among the three subtypes and correlated with patients' overall survival (Zhang et al., 2020). Varshavi et al. performed metabolic characterization of colorectal cancer cells depending on KRAS mutation status using ^{1}H NMR spectra of the metabolites. They revealed that some mutations led to an increase of glucose consumption and lactate release, while others, on the contrary, decreased it (Varshavi et al., 2020). Liu et al. found a correlation between intratumor metabolic heterogeneity parameters of ^{18}F-FDG PET/CT and KRAS mutation status in colorectal cancer – KRAS mutant tumors had more ^{18}F-FDG uptake and heterogeneity than wild-type KRAS (Liu, Wang et al., 2022). In a different study they showed that intratumor metabolic heterogeneity assessed from ^{18}F-FDG PET/CT is an important prognostic factor for progression-free survival and overall survival in patients with colorectal cancer (Liu, Xiang et al., 2022). The value of intratumoral metabolic heterogeneity in ^{18}F-FDG PET/CT for prediction of recurrence in patients with locally advanced colorectal cancer was also demonstrated by Han et al. (Han et al., 2018). In the study by Zhang et al. intratumoral metabolic heterogeneity derived from ^{18}F-FDG PET/CT was higher in colorectal tumors with a high microsatellite instability (MSI) – an important prognostic biomarker, and predicted MSI in stage I–III colorectal cancer patients preoperatively (Zhang et al., 2023). Lin et al. identified two subtypes of colorectal cancer using a metabolic risk score based on genes that were mostly involved in lipid metabolism pathways; this criterion was applied for survival prediction – patients with a higher metabolic risk score had worse prognosis (Lin et al., 2021). Therefore, these clinical studies consider intratumor metabolic heterogeneity as a useful prognostic factor. Our results on patients' colorectal tumors revealed some associations between cell-level heterogeneity and tumor differentiation grade, a stage-independent prognostic factor in colorectal cancer where the lower grade correlates with better

the prognosis. The high-grade (G3) tumors had significantly higher heterogeneity, quantified by the dispersion parameter D NAD(P)H-a_1, compared with low-grade ones.

Another important observation in our research is that bimodality in NAD(P)H-a_1 distribution in primary tumors was linked to the presence of metastases. Several studies report on the correlations of colon tumor heterogeneity with metastases status. For example, in Ref. (Rajput et al., 2017), analysis of the mutational spectra of stage II and III colon cancer samples using next-generation sequencing approach revealed that there was a strong correlation between higher MATH (the Mutant-Allele Tumor Heterogeneity) score and a risk of metastases. Oh et al. observed a significant difference in progression-free survival according to heterogeneity assessment from targeted deep sequencing data, suggesting that tumor heterogeneity might be a determining factor for recurrence or metastasis in colorectal cancer patients with curative resection (Oh et al., 2019). Joung et al., using the whole-exome sequencing, determined that heterogeneity of primary colorectal tumors can predict the potential for liver metastasis (Joung et al., 2017). Similar results were obtained for different types of tumors, including breast (Yang et al., 2017; Chung et al., 2017) and cervical cancers (Kidd and Grigsby, 2008; Pinho et al., 2020).

In the context of metabolic heterogeneity assay using NAD(P)H FLIM, some limitations should be mentioned. If the investigation of patients' tumor metabolism is performed on ex vivo tissue samples, one should be careful to work with freshly excised tissue or store the sample in the appropriate conditions. As we found previously, FLIM parameters of autofluorescence change very quickly (within 15 min) on air, but can be preserved in 10% BSA on ice during 3 h (Lukina et al., 2019). A limitation of our study is that microscopic FLIM images of the tissues were processed manually to obtain information about each individual cell, which made the analysis time-consuming. The methods for segmentation of tissue images have been continuously developed in digital histopathology. As for FLIM, there are approaches to automatic segmentation of FLIM images of cell cultures on the basis of machine learning. So, in spite of the complex and heterogeneous tissue architecture, there are expectations that the task of identification of the individual cells in FLIM images of tissues will be solved in the nearest future. Finally, a small size of the microscopic field of view (typically less 300 µm) limits the inspected area within the tumor sample. Taking into account a high spatial heterogeneity of clinical tumors, there is no confidence whether the inspected area is sufficiently representative.

Owing to the high (sub)cellular resolution (~200–500 nm), FLIM-microscopy provides unique information about metabolic heterogeneity, unavailable with any other methods, like ^{18}F-FDG PET or spatial transcriptomics. Therefore, FLIM-microscopy of endogenous cofactors is not only a powerful research technique, which is capable of improving our understanding of

cellular metabolic diversity, but also the tool with a great potential for clinical translation to predict disease outcome.

Conclusions

It is now evident that metabolic processes in cancer are highly variable, which make the tumor metabolism extremely heterogeneous. Metabolic heterogeneity of tumors complicates treatment efforts and is thought to be a negative prognostic factor. Due to the lack of methods for direct observation and quantification of metabolic heterogeneity at cellular level, it has been poorly characterized so far. Our assessments of cell-level heterogeneity from FLIM-microscopy of NAD(P)H clearly show that heterogeneous metabolic landscape of a patient' tumor is hardly reproducible in in vitro and in vivo models, which underlie the importance of such investigations on clinical material. Although the present research included a limited number of patients (n=21), the obtained results showing the associations between metabolic heterogeneity and clinical features of tumors allow us to consider it as a potential prognostic marker. We plan to continue this study to collect more tumor samples and estimate the correlations between their metabolic heterogeneity and follow-up clinical outcomes.

Materials and methods

Cell Cultures. The human colorectal carcinoma cell lines HT29, HCT116, CaCo2 and murine colon carcinoma cell line CT26 were used in the study. Cells were grown in Dulbecco's modified Eagle's medium (DMEM) (Gibco, Carlsbad, CA, USA) supplemented with 10% fetal bovine serum (FBS) (Gibco, Carlsbad, CA, USA), 2 mM glutamine (Gibco, Carlsbad, CA, USA), 10 mg/mL penicillin (Gibco, Carlsbad, CA, USA), 10 mg/mL streptomycin (Gibco, Carlsbad, CA, USA). The cells were incubated at 37 °C, 5% CO2, and 80% relative humidity and passaged three times a week. The passaging of cells was carried out at a confluence of 70–80% with trypsin-EDTA (Thermo Fisher Scientific, Waltham, MA, USA).

For fluorescence microscopic studies the cells were seeded in 35 mm glass-bottomed FluoroDishes (Ibidi GmbH, Gräfelfing, Germany) in the amount of $5x10^5$ cells in 2 mL of DMEM and incubated for 24 h (37°C, 5% CO2). Before FLIM, DMEM was replaced with the FluoroBrite DMEM (Thermo Fisher Scientific, Waltham, MA, USA) for fluorescence imaging.

Tumor Models. In vivo experiments were performed on female nude and Balb/C mice weighing ~20–22 g. All animal protocols were approved by the Local Ethical Committee of the Privolzhsky Research Medical University (Nizhny Novgorod, Russia). To generate tumors, the suspensions of cancer cells were injected subcutaneously into the tight in the following amount: 1.5×10^6 of HT29 cells in 100 μL PBS, 1.0×10^6 of HCT116 cells in 100 μL PBS, 5.5×10^6 of CaCo2 cells in 100 μL PBS. CT26 cells (2.0×10^5 cells in 20 μL PBS) were inoculated intracutaneously in the ear. The tumor volume was measured using a caliper, and calculated

using the formula v=a×b×1/2b, where a is the length and b is the width of the tumor. In vivo studies were done on 21st day of growth for HT29 tumors (244.8±36.6 mm^3), on the day 23 for HCT116 (533.9±42.0 mm^3), on the day 68 for CaCo2 (397.8±65.2 mm^3), and on the day 14 for CT26 (60.9±5.6 mm^3).

Mice were anesthetized by an intramuscular injection of Zoletil (40 mg/kg, Virbac SA, France) and 2% Rometar (10 mg/kg, Spofa, Czech Republic) for intravital microscopy. The skin over the tumor was opened and covered with a coverslip.

Patient samples. Twenty-one surgical samples of patients' colorectal tumors were obtained in the Nizhny Novgorod Regional Oncological Center (Nizhny Novgorod, Russia) during the tumor resection. All the patients gave informed written consent prior to the enrollment in the study.

All the patients had a histological verification of colorectal adenocarcinoma, the stage definition according to the TNM system, and the definition of the grade. There were tumors of the I–IV stage of low (G1), moderate (G2) and high (G3) grade. The tumors were localized in different sites of the large intestine (caecum, colon, rectum). 19 of 21 patients did not receive any anti-cancer therapy before the surgery, 2 patients (7 and 8) have been pretreated with radiotherapy or chemotherapy. The detailed information about patients' tumors is presented in Table 2, data about their clinicopathological characteristics is presented in Table S2.

Immediately after surgical excision, tumor samples, 0.5–1 cm^3 in size, were wrapped in gauze soaked in a solution of 10% BSA (bovine serum albumin), placed in sterile Petri dish on ice, transferred to the laboratory within 30 min and examined on the laser scanning microscope immediately. This storage protocol allows to preserve autofluorescence lifetime parameters unchanged for at least 3 hours (Lukina et al., 2019).

FLIM-microscopy. FLIM of NAD(P)H was performed using the laser scanning microscope LSM 880 (Carl Zeiss, Germany) equipped with a TCSPC-based FLIM module (Becker & Hickl GmbH, Germany). The Ti:Sa femtosecond laser MaiTai HP (Spectra-Physics Inc., USA, repetition rate 80 MHz, pulse duration 120 fs) was used for two-photon excitation of NAD(P)H at a wavelength of 750 nm. Fluorescence signal was registered in the range 450–490 nm. The laser power applied to the samples was ~6 mW. FLIM images were obtained using the water-immersion objective C-Apochromat W Korr 40×/1.3 (Carl Zeiss, Germany). Image collection time was 60 s. In total, 5–10 images were obtained from each sample.

FLIM images were processed in the SPCImage 8.5 software (Becker & Hickl GmbH, Germany). NAD(P)H fluorescence was analyzed in the cytoplasm of individual cells, in total 50-200 cells in each sample. Fluorescence decay curves were fitted by a bi-exponential model with a goodness of fit χ^2 0.8–1.2. The following fluorescence decay parameters were analyzed: short

component corresponding to the free form of NAD(P)H (τ_1), long component corresponding to the protein-bound NAD(P)H (τ_2), their relative contributions (a_1 и a_2, correspondingly, $a_1+a_2=100\%$), and the mean fluorescence lifetime ($\tau_m = \frac{a_1 \times \tau_1 + a_2 \times \tau_2}{a_1 + a_2}$).

Histopathology and Immunohistochemistry (IHC). Formalin-fixed tumor samples were embedded in paraffin according to standard procedure and cut parallel to the optical plane. The sequential sections 7 µm thick were stained with hematoxylin and eosin, sections 4 µm thick were used for immunohistochemical staining. Sections were stained with primary antibodies to EpCAM (ThermoFisher Scientific, mouse, cat. #14-9326-82, dilution 1:700) and vimentin (Abcam, ab137321, rabbit, dilution 1:700), according to the manufacturer's protocol. Secondary antibodies goat anti-mouse (Alexa Fluor 488) and goat anti-rabbit (Alexa Fluor 555) were used. Tissue sections were imaged using EVOS M7000 Imaging System (Thermo Fisher Scientific Inc., Waltham, MA USA) with LED cubes GFP (ex.470/22 nm, em.510/42 nm for Alexa 488) and RFP (ex.531/40 nm, em. 593/40 nm for Alexa 555) at x20 magnification.

Statistical Analysis. The obtained data were checked for the normal distribution using the Kolmogorov–Smirnov's criterion. The data with a normal distribution were presented as mean ± standard deviation (SD). The data with an abnormal distribution were presented as a median and 25% and 75% quantiles (Q_1 and Q_3). The ANOVA test for comparison data with a normal distribution and the Kruskal-Wallis's test for comparison data with an abnormal distribution were used, with p-val<0.05 being considered statistically significant. Statistical data processing was performed in IBM SPSS Statistics 26.0, R-studio, Python.

Bimodality Index and Dispersity calculation

A continuous measure known as the «bimodality index» is utilized to gauge the degree of conformity of a set of univariate data to a two-component mixture model. The score is larger if the two components are balanced in size or if the separation between the two modes is larger. The BI≥1.1 is considered as a cutoff to reliably define a bimodal distribution in the data (Wang et al., 2009; Shirshin et al., 2022).

BI was calculated according to the equation:

$$BI = \delta \times \sqrt{p(1-p)}, \delta = \frac{|\mu_1 - \mu_2|}{\sqrt{\sigma_1 \sigma_2}}, p = \frac{n_1}{n_1 + n_2},$$

where μ – the mean of each Gaussian, σ – the standard deviation of each Gaussian and n – the number of measurements of each Gaussian.

Dispersion was calculated as interquartile range: 75% quantile – 25% quantile ($Q_3 - Q_1$).

The parameters τ_m and a_1 obtained by FLIM microscopy were used to calculate the bimodality indices (BI) and the dispersion for cultured cells, mouse tumors and patients' samples.

The resulting BI for τ_m and a_1 and dispersion of a_1 were used to search for the relationships between them and the pathophysiological parameters of tumors: the TNM stage and the grade (G).

The fluorescence decay parameters were normalized using the z-normalization method to level out the numerical difference.

A random forest decision tree model was used to evaluate the importance of fluorescence decay parameters on clinicopathological characteristics. The outcome of the model was used for SHAP analysis. Finally, SHAP analysis allowed us to determine the most significant parameters that were investigated by the classic statistical methods (Mann–Whitney).

SHAP (SHapley Additive exPlanations) analysis is a method used to explain the output of any machine learning model. SHAP analysis portrays the relative impact of variables on the output of the model, and it can give insights into the most significant factors and the influence of variables on the result. SHAP values are a way to explain the contribution of each feature to the model's output. They measure how much each feature contributes to the model's prediction and can help identify which features are most important for the model and how they affect the outcome.

The T parameter from TNM was modified in a way that classes 1+2 became group 0, and 3+4 became group 1. The modification of the parameter G resulted in two classes: classes 1+2 became group 0 and class 3 became group 1. Parameters N and M were modified as NM, in which the class was distinguished: no metastases – 0, metastases – 1. Since the clinical parameters, in a modified form, are binary, a point-biserial correlation coefficient was chosen to assess the correlation.

Acknowledgements

The authors are grateful to Dr. Anton Plekhanov (PRMU) for helpful discussions and valuable suggestions.

Funding

This work was supported by the Russian Science Foundation (Project No. 23-15-00294).

Competing interests

The authors declare no conflict of interest.

References

Auman JT, McLeod HL. 2010. Colorectal Cancer Cell Lines Lack the Molecular Heterogeneity of Clinical Colorectal Tumors. *Clinical Colorectal Cancer* **9**:40–47. doi:10.3816/CCC.2010.n.005

Burkel BM, Inman DR, Virumbrales-Muñoz M, Hoffmann EJ, Ponik SM. 2022. A Label-Free Segmentation Approach for Intravital Imaging of Mammary Tumor Microenvironment. *JoVE* 63413. doi:10.3791/63413

Chacko JV, Eliceiri KW. 2019. Autofluorescence lifetime imaging of cellular metabolism: Sensitivity toward cell density, pH, intracellular, and intercellular heterogeneity. *Cytometry Pt A* **95**:56–69. doi:10.1002/cyto.a.23603

Chung YR, Kim HJ, Kim YA, Chang MS, Hwang K-T, Park SY. 2017. Diversity index as a novel prognostic factor in breast cancer. *Oncotarget* **8**:97114–97126. doi:10.18632/oncotarget.21371

DeBerardinis RJ, Chandel NS. 2016. Fundamentals of cancer metabolism. *Sci Adv* **2**:e1600200. doi:10.1126/sciadv.1600200

Evers TMJ, Hochane M, Tans SJ, Heeren RMA, Semrau S, Nemes P, Mashaghi A. 2019. Deciphering Metabolic Heterogeneity by Single-Cell Analysis. *Anal Chem* **91**:13314–13323. doi:10.1021/acs.analchem.9b02410

Farhadi P, Yarani R, Valipour E, Kiani S, Hoseinkhani Z, Mansouri K. 2022. Cell line-directed breast cancer research based on glucose metabolism status. *Biomedicine & Pharmacotherapy* **146**:112526. doi:10.1016/j.biopha.2021.112526

Gentric G, Mieulet V, Mechta-Grigoriou F. 2017. Heterogeneity in Cancer Metabolism: New Concepts in an Old Field. *Antioxidants & Redox Signaling* **26**:462–485. doi:10.1089/ars.2016.6750

Georgakoudi I, Quinn KP. 2023. Label-Free Optical Metabolic Imaging in Cells and Tissues. *Annu Rev Biomed Eng* **25**:413–443. doi:10.1146/annurev-bioeng-071516-044730

Gillette AA, Babiarz CP, VanDommelen AR, Pasch CA, Clipson L, Matkowskyj KA, Deming DA, Skala MC. 2021. Autofluorescence Imaging of Treatment Response in Neuroendocrine Tumor Organoids. *Cancers* **13**:1873. doi:10.3390/cancers13081873

Han Y-H, Jeong H-J, Sohn M-H, Lim ST. 2018. Clinical value of intratumoral metabolic heterogeneity in [18F]FDG PET/CT for prediction of recurrence in patients with locally advanced colorectal cancer. *Q J Nucl Med Mol Imaging* **62**. doi:10.23736/S1824-4785.16.02862-4

Heaster TM, Landman BA, Skala MC. 2019. Quantitative Spatial Analysis of Metabolic Heterogeneity Across in vivo and in vitro Tumor Models. *Front Oncol* **9**:1144. doi:10.3389/fonc.2019.01144

Heaton AR, Rehani PR, Hoefges A, Lopez AF, Erbe AK, Sondel PM, Skala MC. 2023. Single cell metabolic imaging of tumor and immune cells in vivo in melanoma bearing mice. *Front Oncol* **13**:1110503. doi:10.3389/fonc.2023.1110503

Huang D, Ma N, Li X, Gou Y, Duan Y, Liu B, Xia J, Zhao X, Wang X, Li Q, Rao J, Zhang X. 2023. Advances in single-cell RNA sequencing and its applications in cancer research. *J Hematol Oncol* **16**:98. doi:10.1186/s13045-023-01494-6

Joung J-G, Oh BY, Hong HK, Al-Khalidi H, Al-Alem F, Lee H-O, Bae JS, Kim J, Cha H-U, Alotaibi M, Cho YB, Hassanain M, Park W-Y, Lee WY. 2017. Tumor Heterogeneity Predicts Metastatic Potential in Colorectal Cancer. *Clinical Cancer Research* **23**:7209–7216. doi:10.1158/1078-0432.CCR-17-0306

Kidd EA, Grigsby PW. 2008. Intratumoral Metabolic Heterogeneity of Cervical Cancer. *Clinical Cancer Research* **14**:5236–5241. doi:10.1158/1078-0432.CCR-07-5252

Kim J, DeBerardinis RJ. 2019. Mechanisms and Implications of Metabolic Heterogeneity in Cancer. *Cell Metabolism* **30**:434–446. doi:10.1016/j.cmet.2019.08.013

Lakowicz JR, Szmacinski H, Nowaczyk K, Johnson ML. 1992. Fluorescence lifetime imaging of free and protein-bound NADH. *Proc Natl Acad Sci U S A.* **89**:1271-5. doi: 10.1073/pnas.89.4.1271

Lea T. 2015. Caco-2 Cell Line In: Verhoeckx K, Cotter P, López-Expósito I, Kleiveland C, Lea T, Mackie A, Requena T, Swiatecka D, Wichers H, editors. The Impact of Food Bioactives on Health. Cham: Springer International Publishing. pp. 103–111. doi:10.1007/978-3-319-16104-4_10

Lin D, Fan W, Zhang R, Zhao E, Li P, Zhou W, Peng J, Li L. 2021. Molecular subtype identification and prognosis stratification by a metabolism-related gene expression signature in colorectal cancer. *J Transl Med* **19**:279. doi:10.1186/s12967-021-02952-w

Liu X, Wang S-C, Ni M, Xie Q, Zhang Y-F, Lv W-F, Geng G-Y. 2022a. Correlation between 18F-FDG PET/CT intra-tumor metabolic heterogeneity parameters and KRAS mutation in colorectal cancer. *Abdom Radiol* **47**:1255–1264. doi:10.1007/s00261-022-03432-5

Liu X, Xiang K, Geng G-Y, Wang S-C, Ni M, Zhang Y-F, Pan H-F, Lv W-F. 2022b. Prognostic Value of Intratumor Metabolic Heterogeneity Parameters on 18F-FDG PET/CT for Patients with Colorectal Cancer. *Contrast Media & Molecular Imaging* **2022**:1–11. doi:10.1155/2022/2586245

Lukina MM, Dudenkova VV, Ignatova NI, Druzhkova IN, Shimolina LE, Zagaynova EV, Shirmanova MV. 2018. Metabolic cofactors NAD(P)H and FAD as potential indicators of cancer cell response to chemotherapy with paclitaxel. *Biochimica et Biophysica Acta (BBA) - General Subjects* **1862**:1693–1700. doi:10.1016/j.bbagen.2018.04.021

Lukina MM, Shimolina LE, Kiselev NM, Zagainov VE, Komarov DV, Zagaynova EV, Shirmanova MV. 2019. Interrogation of tumor metabolism in tissue samples *ex vivo* using fluorescence lifetime imaging of NAD(P)H. *Methods Appl Fluoresc* **8**:014002. doi:10.1088/2050-6120/ab4ed8

Marusyk A, Polyak K. 2010. Tumor heterogeneity: Causes and consequences. *Biochimica et Biophysica Acta (BBA) - Reviews on Cancer* **1805**:105–117. doi:10.1016/j.bbcan.2009.11.002

Masson N, Ratcliffe PJ. 2014. Hypoxia signaling pathways in cancer metabolism: the importance of co-selecting interconnected physiological pathways. *Cancer Metab* **2**:3. doi:10.1186/2049-3002-2-3

Oh BY, Shin H-T, Yun JW, Kim K-T, Kim J, Bae JS, Cho YB, Lee WY, Yun SH, Park YA, Park YH, Im Y-H, Lee J, Joung J-G, Kim HC, Park W-Y. 2019. Intratumor heterogeneity inferred from targeted deep sequencing as a prognostic indicator. *Sci Rep* **9**:4542. doi:10.1038/s41598-019-41098-0

Parshina YP, Komarova AD, Bochkarev LN, Kovylina TA, Plekhanov AA, Klapshina LG, Konev AN, Mozherov AM, Shchechkin ID, Sirotkina MA, Shcheslavskiy VI, Shirmanova MV. 2022. Simultaneous Probing of Metabolism and Oxygenation of Tumors In Vivo Using FLIM of NAD(P)H and PLIM of a New Polymeric Ir(III) Oxygen Sensor. *IJMS* **23**:10263. doi:10.3390/ijms231810263

Pavlova NN, Thompson CB. 2016. The Emerging Hallmarks of Cancer Metabolism. *Cell Metabolism* **23**:27–47. doi:10.1016/j.cmet.2015.12.006

Pinho DF, King B, Xi Y, Albuquerque K, Lea J, Subramaniam RM. 2020. Value of Intratumoral Metabolic Heterogeneity and Quantitative ^{18}F-FDG PET/CT Parameters in Predicting Prognosis for Patients With Cervical Cancer. *American Journal of Roentgenology* **214**:908–916. doi:10.2214/AJR.19.21604

Plathow C, Weber WA. 2008. Tumor Cell Metabolism Imaging. *J Nucl Med* **49**:43S-63S. doi:10.2967/jnumed.107.045930

Rajput A, Bocklage T, Greenbaum A, Lee J-H, Ness SA. 2017. Mutant-Allele Tumor Heterogeneity Scores Correlate With Risk of Metastases in Colon Cancer. *Clinical Colorectal Cancer* **16**:e165–e170. doi:10.1016/j.clcc.2016.11.004

Sengupta D, Pratx G. 2016. Imaging metabolic heterogeneity in cancer. *Mol Cancer* **15**:4. doi:10.1186/s12943-015-0481-3

Seth Nanda C, Venkateswaran SV, Patani N, Yuneva M. 2020. Defining a metabolic landscape of tumours: genome meets metabolism. *Br J Cancer* **122**:136–149. doi:10.1038/s41416-019-0663-7

Shah AT, Diggins KE, Walsh AJ, Irish JM, Skala MC. 2015. In Vivo Autofluorescence Imaging of Tumor Heterogeneity in Response to Treatment. *Neoplasia* **17**:862–870. doi:10.1016/j.neo.2015.11.006

Shah AT, Heaster TM, Skala MC. 2017. Metabolic Imaging of Head and Neck Cancer Organoids. *PLoS ONE* **12**:e0170415. doi:10.1371/journal.pone.0170415

Sharick JT, Jeffery JJ, Karim MR, Walsh CM, Esbona K, Cook RS, Skala MC. 2019. Cellular Metabolic Heterogeneity In Vivo Is Recapitulated in Tumor Organoids. *Neoplasia* **21**:615–626. doi:10.1016/j.neo.2019.04.004

Sharick JT, Walsh CM, Sprackling CM, Pasch CA, Pham DL, Esbona K, Choudhary A, Garcia-Valera R, Burkard ME, McGregor SM, Matkowskyj KA, Parikh AA, Meszoely IM, Kelley MC, Tsai S, Deming DA, Skala MC. 2020. Metabolic Heterogeneity in Patient Tumor-Derived Organoids by Primary Site and Drug Treatment. *Front Oncol* **10**:553. doi:10.3389/fonc.2020.00553

Shirmanova M, Sergeeva T, Druzhkova I, Meleshina A, Lukina M, Dudenkova V, Shcheslavskiy V, Becker W, Belousov V, Mishina N, Zagaynova E. 2018. 10 Metabolic shifts in cell proliferation and differentiation In: König K, editor. Multiphoton Microscopy and Fluorescence Lifetime Imaging. De Gruyter. pp. 189–208. doi:10.1515/9783110429985-012

Shirmanova MV, Gorbachev DA, Sarkisyan KS, Parnes AP, Gavrina AI, Polozova AV, Kovaleva TF, Snopova LB, Dudenkova VV, Zagaynova EV, Lukyanov KA. 2021. FUCCI-Red: a single-color cell cycle indicator for fluorescence lifetime imaging. *Cell Mol Life Sci* **78**:3467–3476. doi:10.1007/s00018-020-03712-7

Shirmanova MV, Sinyushkina SD, Komarova AD. 2023. Metabolic Heterogeneity of Tumors. *Molecular Biology* **57**(6):1125–1142. doi:10.31857/S0026898423060186.

Shirshin EA, Shirmanova MV, Gayer AV, Lukina MM, Nikonova EE, Yakimov BP, Budylin GS, Dudenkova VV, Ignatova NI, Komarov DV, Yakovlev VV, Becker W, Zagaynova EV, Shcheslavskiy VI, Scully MO. 2022. Label-free sensing of cells with fluorescence lifetime imaging: The quest for metabolic heterogeneity. *Proc Natl Acad Sci USA* **119**:e2118241119. doi:10.1073/pnas.2118241119

Skala MC, Deming DA, Kratz JD. 2022. Technologies to Assess Drug Response and Heterogeneity in Patient-Derived Cancer Organoids. *Annu Rev Biomed Eng* **24**:157–177. doi:10.1146/annurev-bioeng-110220-123503

Stine ZE, Walton ZE, Altman BJ, Hsieh AL, Dang CV. 2015. MYC, Metabolism, and Cancer. *Cancer Discovery* **5**:1024–1039. doi:10.1158/2159-8290.CD-15-0507

Sun Y, Phipps JE, Meier J, Hatami N, Poirier B, Elson DS, Farwell DG, Marcu L. 2013. Endoscopic Fluorescence Lifetime Imaging for *In Vivo* Intraoperative Diagnosis of Oral Carcinoma. *Microsc Microanal* **19**:791–798. doi:10.1017/S1431927613001530

Varshavi Dorna, Varshavi Dorsa, McCarthy N, Veselkov K, Keun HC, Everett JR. 2020. Metabolic characterization of colorectal cancer cells harbouring different KRAS mutations in codon 12, 13, 61 and 146 using human SW48 isogenic cell lines. *Metabolomics* **16**:51. doi:10.1007/s11306-020-01674-2

Walsh AJ, Castellanos JA, Nagathihalli NS, Merchant NB, Skala MC. 2016. Optical Imaging of Drug-Induced Metabolism Changes in Murine and Human Pancreatic Cancer Organoids Reveals Heterogeneous Drug Response. *Pancreas* **45**:863–869. doi:10.1097/MPA.0000000000000543

Walsh AJ, Cook RS, Sanders ME, Aurisicchio L, Ciliberto G, Arteaga CL, Skala MC. 2014. Quantitative Optical Imaging of Primary Tumor Organoid Metabolism Predicts Drug Response in Breast Cancer. *Cancer Research* **74**:5184–5194. doi:10.1158/0008-5472.CAN-14-0663

Walsh AJ, Cook RS, Skala MC. 2017. Functional Optical Imaging of Primary Human Tumor Organoids: Development of a Personalized Drug Screen. *J Nucl Med* **58**:1367–1372. doi:10.2967/jnumed.117.192534

Wang J, Wen S, Symmans WF, Pusztai L, Coombes KR. 2009. The Bimodality Index: A criterion for Discovering and Ranking Bimodal Signatures from Cancer Gene Expression Profiling Data. *Cancer Inform* **7**:CIN.S2846. doi:10.4137/CIN.S2846

Yang F, Wang Yucai, Li Q, Cao L, Sun Z, Jin J, Fang H, Zhu A, Li Y, Zhang W, Wang Yanru, Xie H, Gustafsson J-Å, Wang S, Guan X. 2017. Intratumor heterogeneity predicts metastasis of triple-negative breast cancer. *Carcinogenesis* **38**:900–909. doi:10.1093/carcin/bgx071

Yoshida GJ. 2015. Metabolic reprogramming: the emerging concept and associated therapeutic strategies. *J Exp Clin Cancer Res* **34**:111. doi:10.1186/s13046-015-0221-y

Yuzhakova D, Kiseleva E, Shirmanova M, Shcheslavskiy V, Sachkova D, Snopova L, Bederina E, Lukina M, Dudenkova V, Yusubalieva G, Belovezhets T, Matvienko D, Baklaushev V. 2022. Highly Invasive Fluorescent/Bioluminescent Patient-Derived Orthotopic Model of Glioblastoma in Mice. *Front Oncol* **12**:897839. doi:10.3389/fonc.2022.897839

Yuzhakova DV, Lukina MM, Sachkova DA, Yusubalieva GM, Baklaushev VP, Mozherov AM, Dudenkova VV, Gavrina AI, Yashin KS, Shirmanova MV. 2023. Development of a 3D Tumor Spheroid Model from the Patient's Glioblastoma Cells and Its Study by Metabolic Fluorescence Lifetime Imaging. *Sovrem Tehnol Med* **15**:28. doi:10.17691/stm2023.15.2.03

Zhang L, Liu Y, Ding Y, Deng Y, Chen H, Hu F, Fan J, Lan X, Cao W. 2023. Predictive value of intratumoral-metabolic heterogeneity derived from 18F-FDG PET/CT in distinguishing microsatellite instability status of colorectal carcinoma. *Front Oncol* **13**:1065744. doi:10.3389/fonc.2023.1065744

Zhang M, Wang H, Peng R, Xu F, Wang F, Zhao Q. 2020. Metabolism-Associated Molecular Classification of Colorectal Cancer. *Front Oncol* **10**:602498. doi:10.3389/fonc.2020.602498

Zhou D, Duan Z, Li Z, Ge F, Wei R, Kong L. 2022. The significance of glycolysis in tumor progression and its relationship with the tumor microenvironment. *Front Pharmacol* **13**:1091779. doi:10.3389/fphar.2022.1091779

Figures

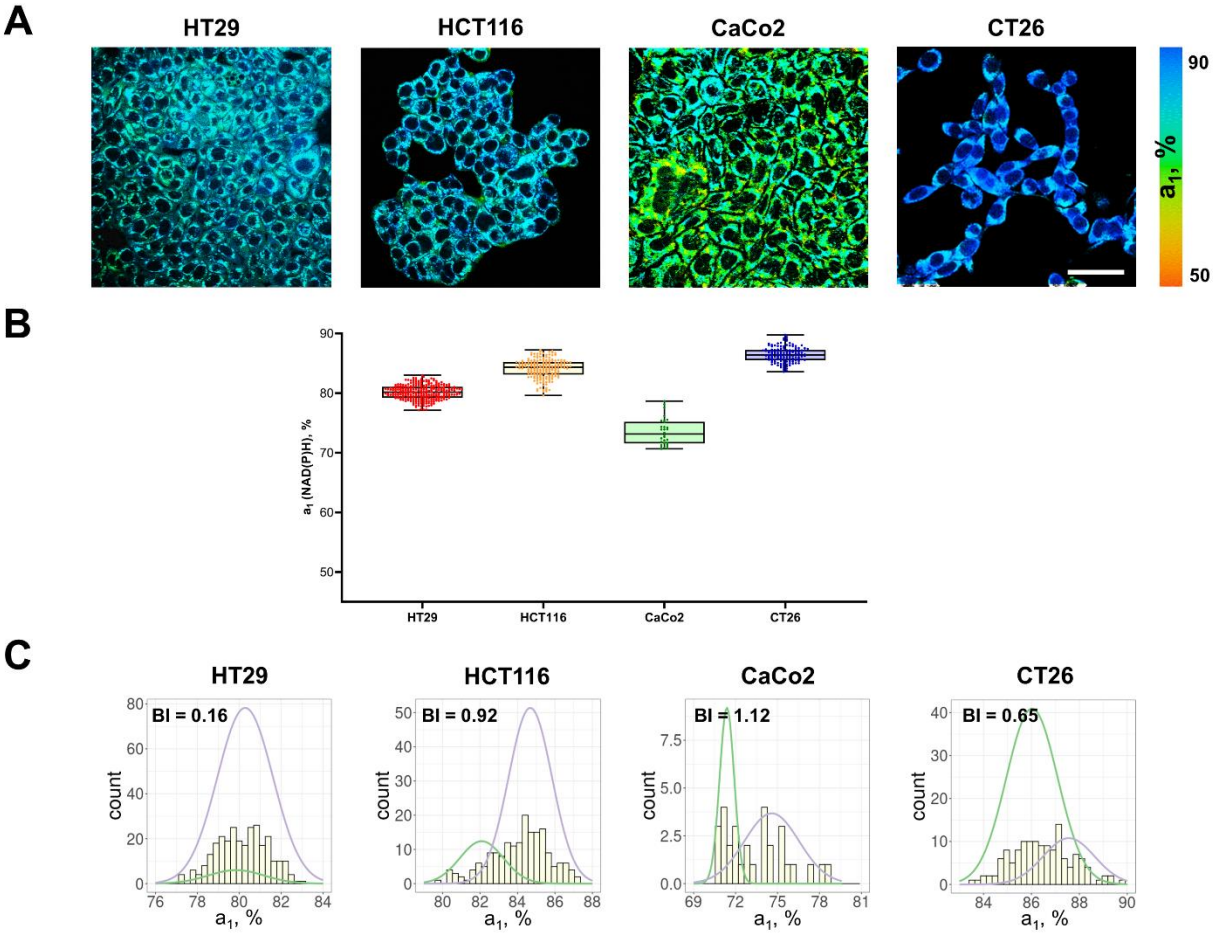

Figure 1. FLIM of NAD(P)H in monolayer cell cultures. (**A**) Representative FLIM images of colorectal cancer cell lines. Scale bar = 50 µm. For FLIM: ex. 750 nm, reg. 450–490 nm. (**B**) The relative contribution of free NAD(P)H (a_1, %) in cell cultures. Box shows the median and the quartiles Q_1 and Q_3, whiskers show minimum and maximum. Dots indicate individual cells (n=280 for HT29 cells, n=185 for HCT116 cells, n=30 for CaCo2 cells, n=138 for CT26 cells). (**C**) The distribution of the NAD(P)H-a_1 for the cell lines. The bimodality index (BI-a_1) is shown on each diagram.

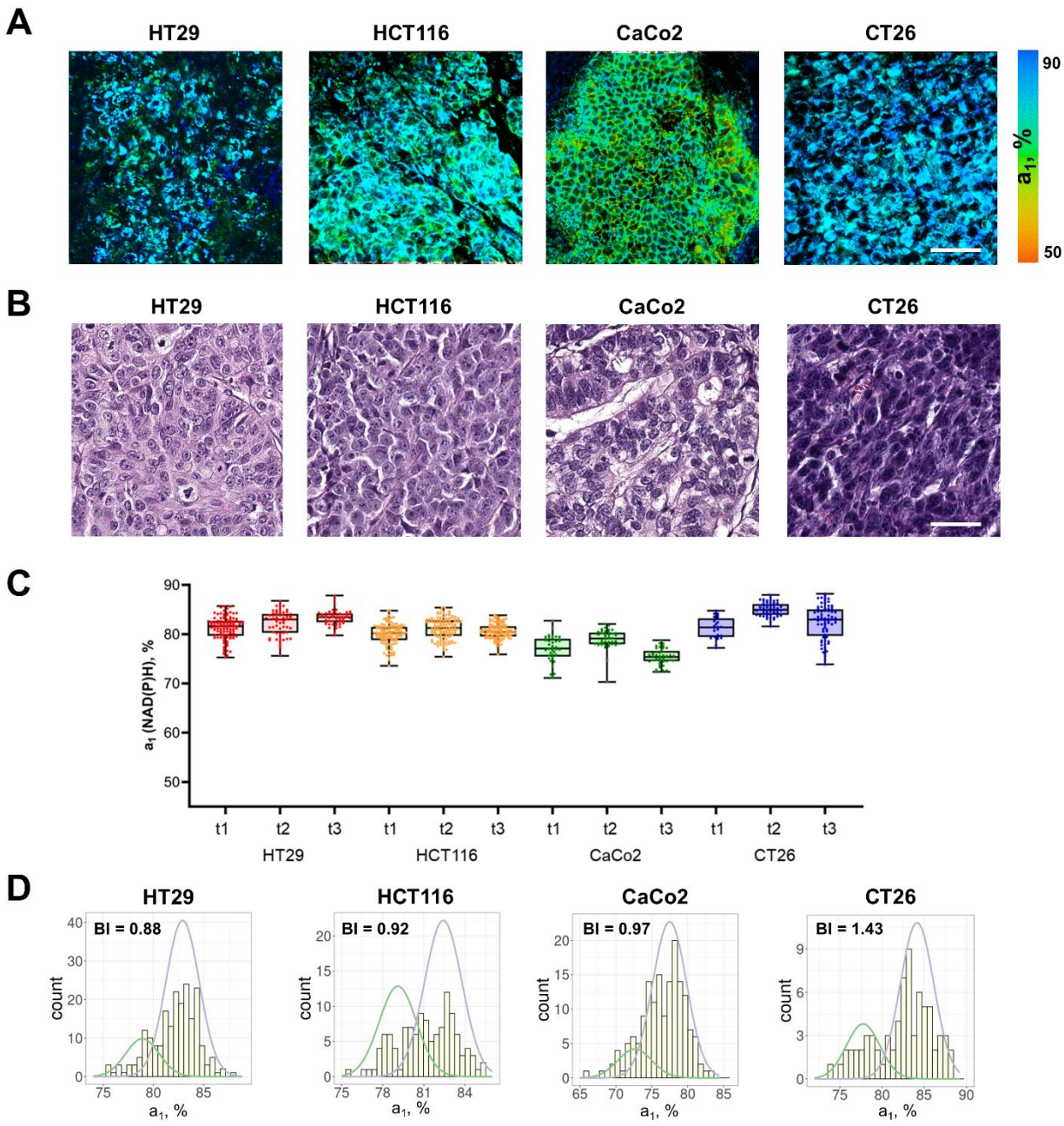

Figure 2. FLIM of NAD(P)H in mouse tumors in vivo. (**A**) FLIM images of NAD(P)H of tumor cells in mouse models in vivo. Scale bar = 50 µm. For FLIM: ex. 750 nm, reg. 450–490 nm. (**B**) Representative histological slices of tumors, hematoxylin/eosin (HE) staining, initial magnification 20×. Scale bar = 50 µm. (**C**) The relative contribution of free NAD(P)H (a_1, %) in tumors (t1, t2, t3) obtained from different cell lines. Box shows the median and the quartiles Q_1 and Q_3, whiskers show minimum and maximum. Dots are the measurements from the individual cells. The bimodality index (BI-a_1) is shown above each box. (**D**) Representative distributions of the NAD(P)H-a_1 for each type of tumor. The bimodality index (BI-a_1) is shown on the diagrams. Dots indicate individual cells (n=280 for HT29, n=340 for HCT116, n=160 for CaCo2, n=350 for CT26).

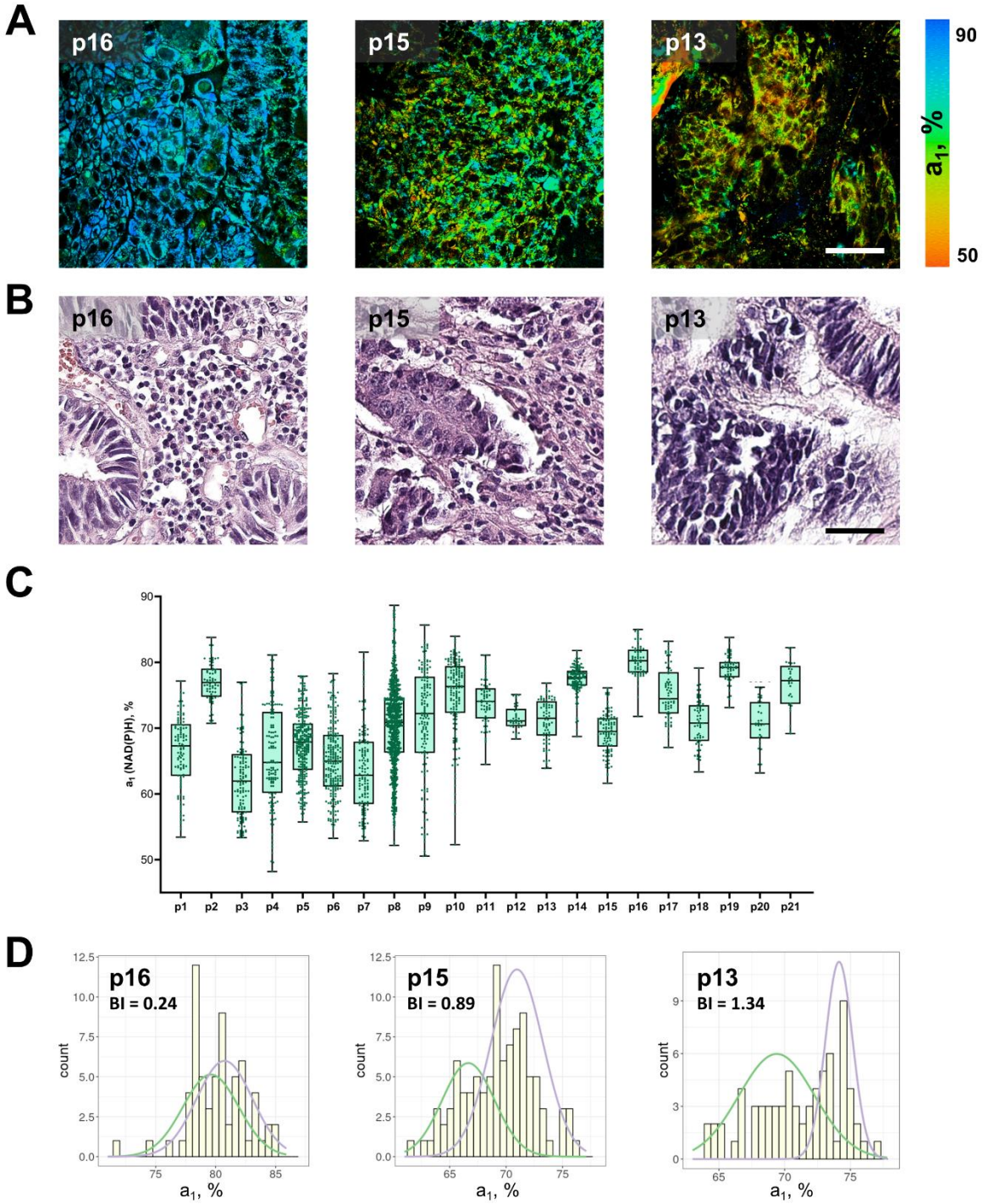

Figure 3. FLIM of NAD(P)H in patients' tumor samples ex vivo. (**A**) Representative FLIM images of tumors. Scale bar = 50 µm. For FLIM: ex. 750 nm, reg. 450–490 nm. (**B**) Histopathology of tumors, hematoxylin/eosin (HE) staining, initial magnification 20×. Scale bar = 50 µm. (**C**) The relative contribution of free NAD(P)H (a_1, %) in patients' tumors (p1–p21). Box shows the median and the quartiles Q_1 and Q_3, whiskers show minimum and maximum. Dots are the measurements from the individual cells. The bimodality index (BI-a_1) is shown above each box. (**D**) Representative distributions of the NAD(P)H-a_1 for patients' tumors.

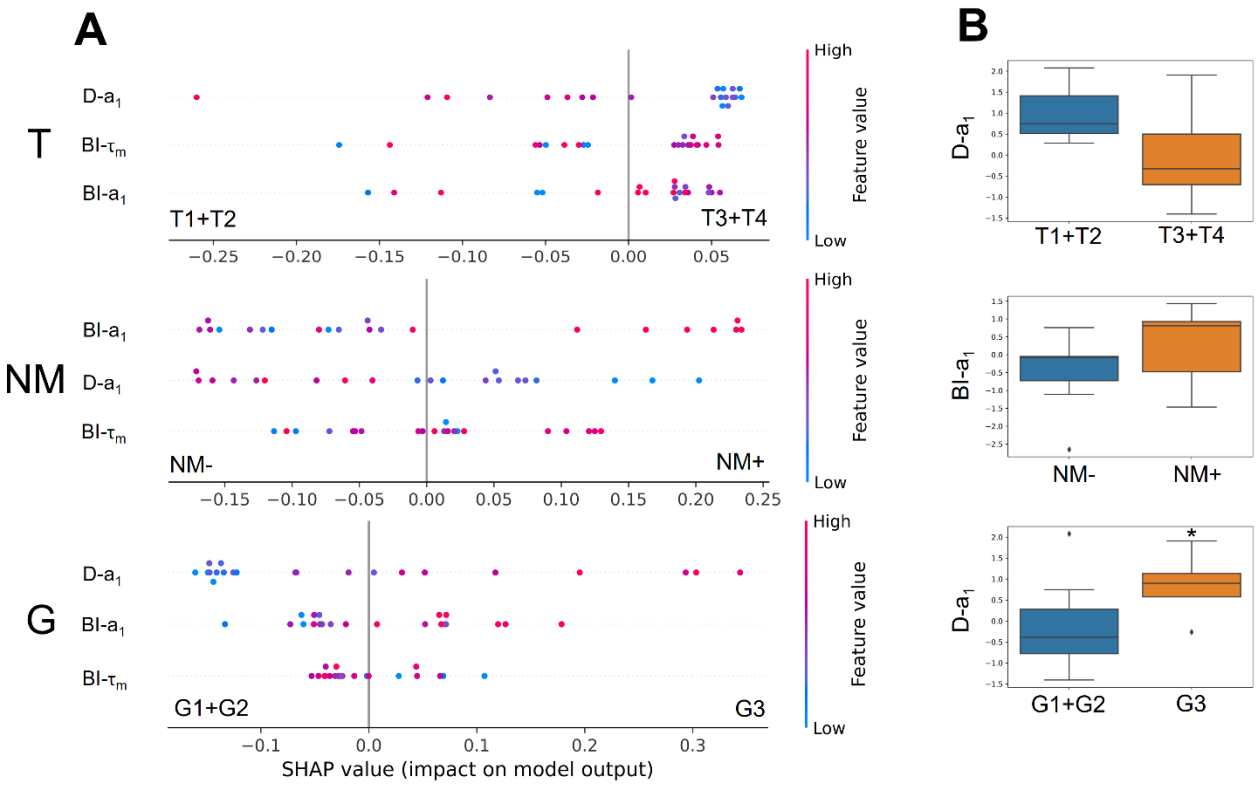

Figure 4. The relationships between fluorescence decay parameters of NAD(P)H and clinicopathological characteristics of patients' tumors. (**A**) Plots of SHAP analysis for the built decision tree models to determine the importance of the parameters. The higher the parameter value, the more red the dot is. (**B**) Box-plots of the selected parameters with highest significance, * p-val < 0.05.

Tables

Table 1. The Bimodality Index BI-a_1 and Dispersity D-a_1 of NAD(P)H in cultured cells, mouse tumors and patients' tumor samples.

	Cell lines in vitro				**Tumors in vivo**			
	HT29	**HCT116**	**CaCo2**	**CT26**	**HT29**	**HCT116**	**CaCo2**	**CT26**
BI-a_1	0.16	0.92	**1.12**	0.65	0.85 ± 0.61	0.93 ± 0.23	0.88 ± 0.13	**1.11 ± 0.51**
D-a_1	1.83	2.01	3.50	1.67	3.20	2.60	4.00	4.02

	Patients' tumors ex vivo																				
Sample	**p1**	**p2**	**p3**	**p4**	**p5**	**p6**	**p7**	**p8**	**p9**	**p10**	**p11**	**p12**	**p13**	**p14**	**p15**	**p16**	**p17**	**p18**	**p19**	**p20**	**p21**
BI-a_1	**1.25**	0.81	1.01	**1.16**	1.01	1.00	0.86	0.70	**1.28**	**1.25**	0.59	**1.45**	**1.34**	1.05	0.89	0.24	**1.29**	**1.32**	0.80	0.94	**1.28**
D-a_1	7.77	4.18	8.68	11.99	6.93	7.83	9.33	8.25	1.51	6.96	4.50	2.37	4.94	2.19	4.16	3.34	6.10	5.41	2.23	5.19	5.27

Table 2. Information about patients and their colorectal tumors.

Characteristics	**Number**	**Percent**
Gender		
Male	10	47.6
Female	11	52.4
Age		
Mean ± SD	64.3 ± 12.3 y.o.	–
Median	65.5 y.o.	–
Tumor staging		
I	3	14.3
IIA	3	14.3
IIB	2	9.5
IIIB	8	38.1
IIIC	1	4.7
IV	4	19.1
Tumor site		
Caecum	2	9.5
Transverse colon	4	19.1
Hepatic flexure	2	9.5
Sigmoid colon	8	38.1
Rectum	5	23.8
Low (G1)	4	19.1
Moderate (G2)	12	57.1
High (G3)	5	23.8

Author information

Anastasia D Komarova
Institute of Experimental Oncology and Biomedical Technologies, Privolzhsky Research Medical University, Nizhny Novgorod, Russia; Institute of Biology and Biomedicine, Lobachevsky State University of Nizhny Novgorod, Nizhny Novgorod, Russia
Contribution: investigation, visualization, writing—original draft
Contributed equally with: Snezhana D Sinyushkina
Competing interests: No competing interests declared
Snezhana D Sinyushkina
Institute of Experimental Oncology and Biomedical Technologies, Privolzhsky Research Medical University, Nizhny Novgorod, Russia
Contribution: investigation, visualization, writing—original draft
Contributed equally with: Anastasia D Komarova
Competing interests: No competing interests declared
Ilia D Shchechkin
Institute of Experimental Oncology and Biomedical Technologies, Privolzhsky Research Medical University, Nizhny Novgorod, Russia; Institute of Biology and Biomedicine, Lobachevsky State University of Nizhny Novgorod, Nizhny Novgorod, Russia
Contribution: investigation, visualization
Competing interests: No competing interests declared
Irina N Druzhkova
Institute of Experimental Oncology and Biomedical Technologies, Privolzhsky Research Medical University, Nizhny Novgorod, Russia
Contribution: funding acquisition, investigation, visualization
Competing interests: No competing interests declared
Sofia A Smirnova
Institute of Experimental Oncology and Biomedical Technologies, Privolzhsky Research Medical University, Nizhny Novgorod, Russia
Contribution: investigation
Competing interests: No competing interests declared
Vitaliy M Terekhov
Surgery department, Nizhny Novgorod Regional Oncologic Hospital, Nizhny Novgorod, Russia
Contribution: investigation
Competing interests: No competing interests declared
Artem M Mozherov

Institute of Experimental Oncology and Biomedical Technologies, Privolzhsky Research Medical University, Nizhny Novgorod, Russia
Contribution: investigation
Competing interests: No competing interests declared
Nadezhda I Ignatova
Institute of Experimental Oncology and Biomedical Technologies, Privolzhsky Research Medical University, Nizhny Novgorod, Russia
Contribution: investigation
Competing interests: No competing interests declared
Elena E Nikonova
Laboratory of Clinical Biophotonics, Sechenov First Moscow State Medical University, Moscow, Russia
Contribution: methodology
Competing interests: No competing interests declared
Evgeny A Shirshin
Laboratory of Clinical Biophotonics, Sechenov First Moscow State Medical University, Moscow, Russia; Faculty of Physics, Lomonosov Moscow State University, Moscow, Russia
Contribution: data curation, methodology, writing—review and editing
Competing interests: No competing interests declared
Vladislav I Shcheslavskiy
Institute of Experimental Oncology and Biomedical Technologies, Privolzhsky Research Medical University, Nizhny Novgorod, Russia; Becker&Hickl GmbH, Germany
Contribution: data curation, validation, writing—review and editing
Competing interests: No competing interests declared
Marina V Shirmanova
Institute of Experimental Oncology and Biomedical Technologies, Privolzhsky Research Medical University, Nizhny Novgorod, Russia
Contribution: conceptualization, data curation, project administration, supervision, writing—original draft, writing—review and editing
For correspondence: Shirmanovam@mail.ru
Competing interests: No competing interests declared

Supplementary

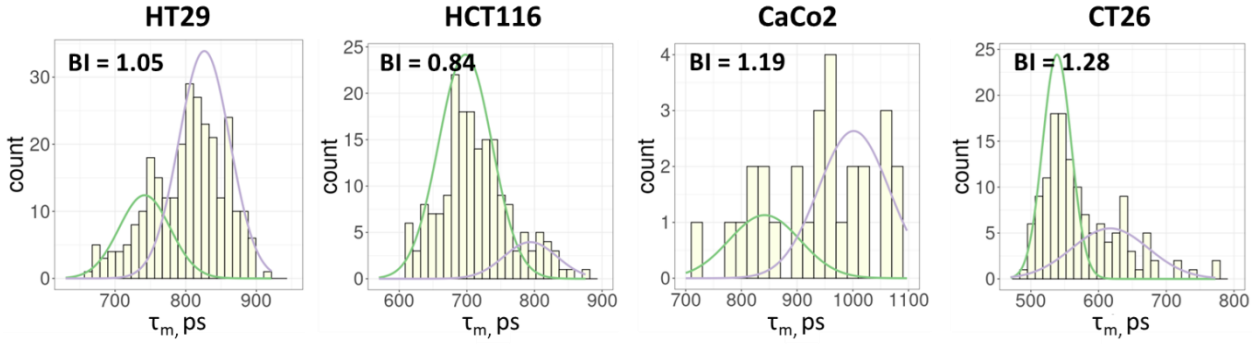

Figure S1. FLIM of NAD(P)H in monolayer cell cultures. The distribution of the NAD(P)H-τ_m for the cell lines. The bimodality index (BI-τ_m) is shown on each diagram.

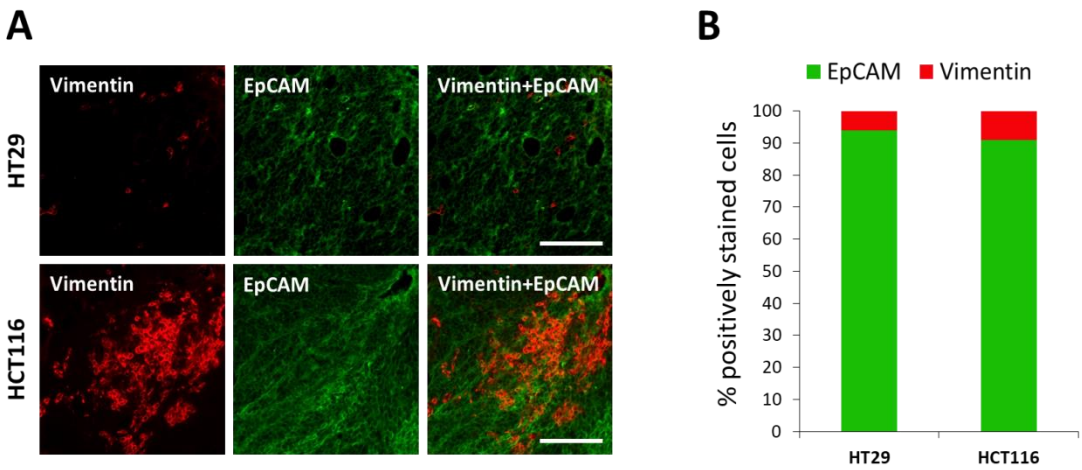

Figure S2. Immunohistochemical analysis of HCT116 and HT29 tumors using primary antibodies to EpCAM (green, epithelial cells marker) and vimentin (red, mesenchymal cells marker). (**A**) Immunofluorescence images of HT29 and HCT116 tumors. Scale bar = 100 μm. (**B**) The ratio of positively stained EpCAM+ and vimentin+ cells in tumor sections.

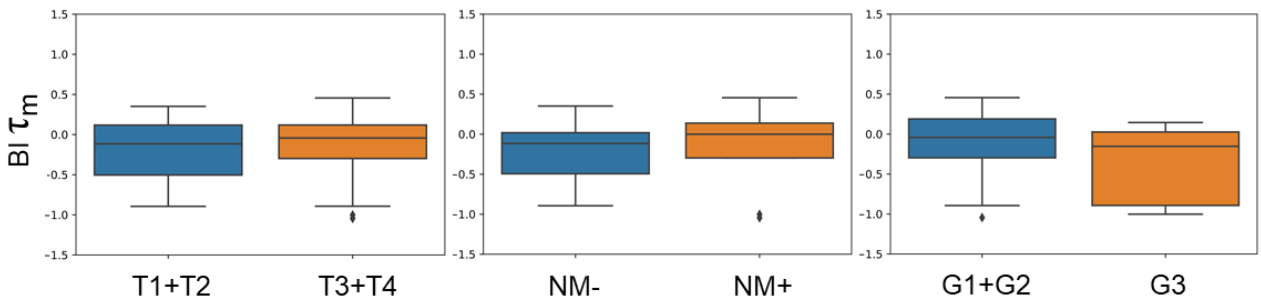

Figure S3. The relationships between parameter BI τ_m and clinicopathological characteristics of patients' tumors. Box-plots of the clinicopathological characteristics and parameter BI-τ_m. No significant differences were found between the groups.

Table S1. NAD(P)H fluorescence decay parameters of colorectal cancer cells in monolayer cultures in vitro and in mouse tumors in vivo.

τ_m – mean lifetime, τ_1 – short lifetime component, τ_2 – long lifetime component, a_1 – relative contribution of the short lifetime component, BI-τ_m – bimodality index of the mean lifetime, BI-a_1 – bimodality index of relative contribution of the short lifetime component, D-a_1 – dispersion of relative contribution of the short lifetime component.

Cell line	**τ_m, ns**	**τ_1, ns**	**τ_2, ns**	**a_1, %**	**BI-τ_m**
Cell lines in vitro					
HT29	0.80±0.05	0.39±0.03	2.47±0.17	80.11±1.34	1.05
HCT116	0.71±0.05	0.40±0.02	2.39±0.20	84.13±1.58	0.84
CaCo2	0.95±0.10	0.38±0,05	2.53±0.24	73.48±2.26	1.19
CT26	0.57±0.06	0.35±0.03	2.03±0.22	86.48±1.28	1.28
Tumors in vivo					
HT29	0.85[0.81;0.90]	0.46[0.45;0.48]	2.70[2.59;2.79]	82.68 [80.79;83.65]	1.13±0.37
HCT116	0.88[0.85;0.92]	0.47[0.45;0.48]	2.67[2.56;2.77]	80.61 [79.32;81.96]	0.91±0.28
CaCo2	1.03[0.92;1.10]	0.44[0.40;0.47]	2.98[2.75;3.12]	76.46 [75.07;78.42]	1.41±0.61
CT26	0.73[0.69;0.78]	0.39[0.37;0.41]	2.38[2.22;2.53]	82.77 [81.05;84.20]	1.12±0.37

Table S2. Clinicopathological characteristics of patients' tumors

№	**Tumor site**	**Tumor type**	**Tumor stage**	**Tumor grade**
1	Rectum colon	Adenocarcinoma	cT4bN1M0 (stage IIIB)	High
2	Sigmoid colon	Serrated Adenocarcinoma	T4aN0M0 (stage IIB)	Moderate
3	Transverse colon	Adenocarcinoma	T4bN0M0 (stage IIB)	High
4	Sigmoid colon	Serrated Adenocarcinoma	T1N0M0 (stage I)	Low
5	Sigmoid colon	Serrated Adenocarcinoma	pT3N0M0 (stage IIA)	Moderate
6	Sigmoid colon	Adenoma-like Adenocarcinoma	pT3bN0M0 (stage IIA)	Moderate
7	Hepatic flexure	Poorly Cohesive Adenocarcinoma	pT4aN0M1c (stage IV)	High
8	Rectum colon	Adenoma-like Adenocarcinoma	pT2N0M0 (stage I)	Moderate
9	Sigmoid colon	Adenocarcinoma	pR0T3N2bM0 (stage IIIC)	High

10	Rectum colon	Adenoma-like Adenocarcinoma	pT2N0M0 (stage I)	Low
11	Sigmoid colon	Adenocarcinoma	T3N1M0 (stage IIIB)	Moderate
12	Transverse colon	Adenocarcinoma	T3N0M1 (stage IV)	Moderate
13	Cecum colon	Adenocarcinoma	T3N1M0 (stage IIIB)	Moderate
14	Rectum colon	Adenocarcinoma	T3N1M0 (stage IIIB)	Moderate
15	Cecum colon	Adenocarcinoma	T3N1M0 (stage IIIB)	Low
16	Rectum colon	Adenocarcinoma	T3N1M0 (stage IIIB)	Moderate
17	Hepatic flexure	Adenocarcinoma	T3N0pM1c (stage IV)	Moderate
18	Transverse colon	Adenocarcinoma	T3N0M1c (stage IV)	High
19	Sigmoid colon	Adenocarcinoma	cT4bN1M0c (stage IIIB)	Moderate
20	Sigmoid colon	Adenocarcinoma	T3N0M0 (stage IIA)	Moderate
21	Transverse colon	Adenocarcinoma	cT3N1M0 (stage IIIB)	Low

Table S3. NAD(P)H fluorescence decay parameters of patients' tumors ex vivo.

№	τ_m, ns	τ_1, ns	τ_2, ns	a_1, %	BI-τ_m
1	1.21[1.08;1.31]	0.50[0.44;0.55]	2.68[2.26;3.01]	67.30[62.74;70.61]	1.15
2	1.03[0.97;1.08]	0.50[0.47;0.52]	2.89[2.65;3.04]	76.92[74.76;79.05]	1.04
3	1.05[0.98;1.12]	0.46[0.42;0.52]	1.99[1.79;2.31]	61.96[57.17;66.07]	0.29
4	0.90[0.83;0.97]	0.41[0.38;0.46]	1.83[1.64;2.15]	64.79[60.15;72.47]	0.93
5	1.00[0.94;1.08]	0.46[0.43;0.50]	2.14[1.85;2.38]	67.88[63.63;70.69]	0.62
6	1.03[0.96;1.11]	0.50[0.46;0.53]	2.06[1.81;2.29]	64.99[61.13;68.97]	0.88
7	1.01[0.92;1.07]	0.45[0.39;0,49]	1.91[1.76;2.14]	62.84[58.47;67.94]	1.05
8	0.98[0.90;1.09]	0.44[0.41;0.49]	2.28[1.99;2.58]	70.85[66.26;74.53	0.29
9	0.86[0.78;0.95]	0.35[0.30;0.39]	2.12[1.76;2.58]	72.20[66.23;77.82]	0.20

10	0.88[0.84;0.98]	0.45[0.42;0.50]	2.31[2.07;2.57]	76.33[72.32;79.41]	1.32
11	1.14[1.04;1.23]	0.49[0.46;0.51]	3.00[2.82;3.18]	74.06[71.47;76.07]	1.08
12	1.20[1.13;1.26]	0.50[0.49;0.52]	2.96[2.82;3.13]	71.08[70.29;72.93]	1.40
13	1.19[1.16;1.23]	0.51[0.42;0.53]	2.98[2.80;3.16]	71.50[68.85;74.09]	1.14
14	1.00[9.70;1.04]	0.47[0.46;0.47]	2.86[2.80;2.95]	77.68[76.47;78.72]	0.78
15	1.30[1.23;1.38]	0.53[0.50;0.57]	3.09[2.86;3.37]	69.49[67.19;71.52]	0.78
16	0.87[0.79;0.97]	0.44[0.41;0.47]	2.67[2.51;2.82]	80.24[78.45;81.91]	0.98
17	1.05[0.94;1.19]	0.43[0.36;0.47]	3.10[2.83;3.21]	74.45[72.21;78.50]	1.00
18	1.23[1.18;1.29]	0.50[0.48;0.52]	3.00[2.87;3.22]	70.76[68.03;73.49]	0.90
19	0.93[0.90;0.97]	0.47[0.44;0.48]	2.75[2.60;2.87]	79.21[77.71;80.05]	1.31
20	0.81[0.74;1.41]	0.23[0.21;0.55]	2.33[2.16;3.23]	70.63[68.41;73.97]	4.24
21	1.13[1.01;1.20]	0.49[0.48;0.52]	3.22[3.03;3.31]	77.22[73.68;79.47]	0.17